Numerical solution of the Dirac equation by a mapped Fourier grid method

Numerical solution of the Dirac equation by a mapped Fourier grid method

E Ackad and M Horbatsch

Department of Physics and Astronomy, York University, 4700 Keele St, Toronto, Ontario, M3J 1P3, Canada

Abstract
An efficient numerical method is developed to solve the relativistic hydrogenic Coulomb problem. Combining a pseudospectral method and a change of coordinates, a matrix representation of the relativistic Hamiltonian is constructed in position space. The radial coordinate is mapped from the semi-infinite r-axis to a finite range. The accuracy of the calculation is tested by comparing eigenvalues, sum rules and eigenfunctions with known analytic results. The method can be applied to central field problems for which analytic solutions are unknown.

PACS numbers: 31.15.−p, 03.65.−w

1. Introduction

The problem of relativistic atomic or molecular structure calculations is reasonably well understood and can be solved at the level of Dirac–Hartree–Fock [1] or density functional theory [2]. The situation is not so obvious for time-dependent problems as they arise in the atom–laser interactions [3] or heavy ion–atom collisions [4]. For these problems it is worthwhile to pursue the so-called spectral methods, most notably Fourier grid techniques. These have been developed in the non-relativistic Schrödinger context, and applied, e.g. to cold atom–atom collisions [5].

In this paper we develop a mapped Fourier grid method for the stationary Dirac problem. We test it on the hydrogenic atom case for which exact analytical results are available. We demonstrate how finite-basis diagonalization of the non-symmetric Hamiltonian matrix yields accurate eigenvalues and eigenfunctions. Thus, the usefulness of the method is established, which, e.g. would permit to extend the Cs–Cs cold collision calculations of [5] to incorporate relativistic atomic structure.

Previously, the mapped Fourier grid method has been proposed for the non-relativistic Schrödinger problem and has been applied successfully in the context of atomic and chemical physics [5–7]. The method was based on the Fourier grid method of Meyer [8] and was

augmented by a mapping of the grid points, thereby enhancing the quality of the sampling of the eigenfunctions. It was shown by Fattal *et al* [9] that this mapping could compensate for problems associated with the singularities of the Coulomb potential. In momentum space a singularity appears as a result of the long-range tail of the Coulomb interaction. By placing more points near the origin in position space, and continuing with a sparse number farther out from the origin both singularity issues are addressed. Consequently, this mapping allows for a better representation of the relevant phase-space region in comparison with the unmapped Fourier grid method, granting a higher efficiency for the same number of grid points.

The problem of how to approximate a non-periodic function by a series of periodic functions was also addressed by Fattal *et al* [9] by extending the radial coordinate (r) range to include negative values, and assuming the function to be exponentially small as $|r| \to \infty$. Thus, the error in approximating the non-periodic function becomes exponentially small. The negative r-values need not be calculated by requiring an antisymmetric mapping and assuming the approximated function to be antisymmetric, which imposes the $f(0) = 0$ boundary condition.

One of the main features of the Fourier method is that the entire calculation can be performed in position space while using an analytic expression for the derivative terms. This is to be contrasted with finite-difference methods or other derivative approximation schemes. Given that the potential is usually given as a function of the coordinates, it is convenient to construct a matrix representation directly in position space without the need to compute matrix elements of the potential. A review of the Fourier method for solving the Schrödinger equation and comparison to other pseudospectral methods is provided in [10].

In this paper the Fourier grid method is extended to the relativistic hydrogenic Coulomb problem by the use of a mapping of the position points. The mapping given in [9] is substantially modified. The relativistic version has many differences from the non-relativistic problem, such as the requirement to deal with a two-component solution with different boundary conditions for each component [11]. Also, the spectrum of the relativistic Hamiltonian is not bounded from below and so it is not possible to use standard variational methods. The method yields a set of eigenstates which may be used, e.g., for time-dependent problems as was done in the non-relativistic case in [12].

In section 2 details are given of how to build the matrix representation of the Dirac–Coulomb Hamiltonian, as well as a motivation for the chosen mapping function. In section 3 we show some results for hydrogen to indicate the level of accuracy that can be achieved with the method. It is shown how the calculation can be adapted to provide accurate bound states by an appropriate choice of the scaling parameters. We also discuss the quality of the eigenvectors and show some results for hydrogen-like ions.

2. The Hamiltonian

The coupled radial Dirac equations for the upper and lower components G and F are commonly written as [13, 14]

$$-c\hbar\frac{\mathrm{d}F}{\mathrm{d}r} - \frac{(1-\kappa)\hbar c}{r}F = (E - V(r) - mc^2)G, \tag{1}$$

$$c\hbar\frac{\mathrm{d}G}{\mathrm{d}r} + \frac{(1+\kappa)\hbar c}{r}G = (E - V(r) + mc^2)F, \tag{2}$$

where κ is a quantum number analogous to the angular momentum quantum number l in non-relativistic quantum mechanics. Using $f(r) = rF(r)$, $g(r) = rG(r)$ and the Coulomb

potential for a charge Z, in relativistic units $\hbar = m_e = c = 1$, the equations become

$$\frac{\mathrm{d}f}{\mathrm{d}r} - \frac{\kappa}{r} f = -\left(E + \frac{Z\alpha}{r} - 1\right) g, \tag{3}$$

$$\frac{\mathrm{d}g}{\mathrm{d}r} + \frac{\kappa}{r} g = \left(E + \frac{Z\alpha}{r} + 1\right) f, \tag{4}$$

where $\alpha = e^2/\hbar c$ is the fine-structure constant. It is useful to write equations (3) and (4) in matrix notation,

$$\begin{pmatrix} -\left(\frac{Z\alpha}{r} - 1\right) & -\left(\frac{\mathrm{d}}{\mathrm{d}r} - \frac{\kappa}{r}\right) \\ \left(\frac{\mathrm{d}}{\mathrm{d}r} + \frac{\kappa}{r}\right) & -\left(\frac{Z\alpha}{r} + 1\right) \end{pmatrix} \begin{pmatrix} g(r) \\ f(r) \end{pmatrix} = E \begin{pmatrix} g(r) \\ f(r) \end{pmatrix}. \tag{5}$$

The mapping for the Schrödinger–Coulomb problem from [9] is modified by introducing an additional scaling parameter s, and a second-order singularity at $\theta = \pi$, giving

$$r(\theta) = \frac{s\theta - A \arctan \frac{s\theta}{A}}{(\pi - \theta)^2}, \tag{6}$$

where we choose $A = 4000$. This choice of A was motivated in [9] by looking at the coverage of the classical phase space for an optimal representation of about 20 bound hydrogenic states. The introduction of the singularity at $\theta = \pi$ does not modify the behaviour at small θ, and thus the choice of $A = 4000$ is also good for our relativistic treatment of hydrogen. The added scale parameter s allows us to tailor the coverage in phase space in order to achieve an optimal representation for more bound states or for a combination of bound and continuum parts of the spectrum. The latter will be important for time-dependent applications where both excitation and ionization are present.

The singularity at $\theta = \pi$ permits to map the semi-infinite r-range to $\theta \in [0, \pi)$. This feature allows us to incorporate the correct boundary condition as $r \to \infty$, which leads to improved orthogonality of the computed eigenstates.

In terms of the independent variable θ, equation (5) becomes,

$$\begin{pmatrix} -\left(\frac{Z\alpha}{r(\theta)} - 1\right) & -\left(\frac{1}{J(\theta)}\frac{\mathrm{d}}{\mathrm{d}\theta} - \frac{\kappa}{r(\theta)}\right) \\ \left(\frac{1}{J(\theta)}\frac{\mathrm{d}}{\mathrm{d}\theta} + \frac{\kappa}{r(\theta)}\right) & -\left(\frac{Z\alpha}{r(\theta)} + 1\right) \end{pmatrix} \begin{pmatrix} g(r(\theta)) \\ f(r(\theta)) \end{pmatrix} = E \begin{pmatrix} g(r(\theta)) \\ f(r(\theta)) \end{pmatrix}, \tag{7}$$

where $J(\theta)$ is the Jacobian of the transformation from r to θ given by

$$J(\theta) = \frac{\mathrm{d}r}{\mathrm{d}\theta} = \frac{s - \frac{s}{1 + (\frac{s\theta}{A})^2}}{(\pi - \theta)^2} + 2\frac{s\theta - A \arctan \frac{s\theta}{A}}{(\pi - \theta)^3}. \tag{8}$$

This Jacobian weakens the singularity in the second derivative at the origin (due to the antisymmetric extension into the $-r$ region) in comparison with the original mapping given by Fattal *et al* [9].

A finite sine series truncated at order N is chosen to represent each component of the spinor, i.e.,

$$\begin{pmatrix} g(r(\theta)) \\ f(r(\theta)) \end{pmatrix} = \begin{pmatrix} \sum_{m=1}^{N} a_m \sin(m\theta) \\ \sum_{n=1}^{N} b_n \sin(n\theta) \end{pmatrix}. \tag{9}$$

Equation (9) when inserted into equation (7) yields an analytic expression for the derivative,

$$\frac{\mathrm{d}}{\mathrm{d}\theta} \begin{pmatrix} \sum_{m=1}^{N} a_m \sin(m\theta) \\ \sum_{n=1}^{N} b_n \sin(n\theta) \end{pmatrix} = \begin{pmatrix} \sum_{m=1}^{N} m a_m \cos(m\theta) \\ \sum_{n=1}^{N} n b_n \cos(n\theta) \end{pmatrix}. \tag{10}$$

In order to solve the problem numerically the θ variable is discretized. The number of points used for the θ mesh is set to N, yielding a square $(2N \times 2N)$ Hamiltonian matrix. The spinor is now represented at $\theta = \theta_i$ by an eigenvector of the Hamiltonian matrix with the two components combined into a vector of length $2N$. The θ_i points are evenly spaced by $\Delta\theta = \frac{\pi}{N+1}$. The furthest point on the mesh is given by $r_{max} = r(N\Delta\theta)$, which is controlled by the scaling parameters. Note that r_{max} increases with s in a nonlinear fashion. Thus, for given N, s determines the number of bound states and pseudo-Rydberg states that are obtained, as well as their respective accuracies.

The expansion coefficients in equation (9) are obtained from projection by the discrete sums:

$$a_k = \frac{2}{N+1} \sum_{j=1}^{N} g(\theta_j) \sin(k\theta_j), \tag{11}$$

and

$$b_k = \frac{2}{N+1} \sum_{j=1}^{N} f(\theta_j) \sin(k\theta_j). \tag{12}$$

The spinor (9) is therefore written explicitly as

$$\begin{pmatrix} \frac{2}{N+1} \sum_{j=1}^{N} \sum_{m=1}^{N} \sin(m\theta_j) \sin(m\theta_i) g(\theta_j) \\ \frac{2}{N+1} \sum_{j=1}^{N} \sum_{n=1}^{N} \sin(n\theta_j) \sin(n\theta_i) f(\theta_j) \end{pmatrix}. \tag{13}$$

Introduction of the cosine–sine matrix,

$$D_{ij} = \frac{2}{N+1} \sum_{m=1}^{N} m \cos(m\theta_i) \sin(m\theta_j), \tag{14}$$

simplifies the discretized equation (10) to

$$\begin{pmatrix} \frac{2}{N+1} \left(\frac{d}{d\theta} \sum_{j=1}^{N} \sum_{m=1}^{N} \sin(m\theta_j) \sin(m\theta) g(\theta_j) \right)_i \\ \frac{2}{N+1} \left(\frac{d}{d\theta} \sum_{j=1}^{N} \sum_{n=1}^{N} \sin(n\theta_j) \sin(n\theta) f(\theta_j) \right)_i \end{pmatrix} = \begin{pmatrix} \frac{2}{N+1} \sum_{j=1}^{N} D_{ij} g(\theta_j) \\ \frac{2}{N+1} \sum_{j=1}^{N} D_{ij} f(\theta_j) \end{pmatrix}, \tag{15}$$

where the index i refers to the fact that the spinor derivative is evaluated at $r = r_i = r(\theta_i)$.

The discretized Hamiltonian is now written in block-component form as

$$\begin{pmatrix} -\left(\frac{Z\alpha}{r(\theta_i)} - 1 \right) \delta_{i,j} & -\left(\frac{D_{ij}}{J(\theta_i)} - \frac{\kappa\delta_{i,j}}{r(\theta_i)} \right) \\ \left(\frac{D_{ij}}{J(\theta_i)} + \frac{\kappa\delta_{i,j}}{r(\theta_i)} \right) & -\left(\frac{Z\alpha}{r(\theta_i)} + 1 \right) \delta_{i,j} \end{pmatrix}. \tag{16}$$

Due to the derivative terms, the representation of the Hamiltonian in the Fourier-sine basis is non-symmetric. In practice, one should be concerned about the appearance of complex eigenvalues mostly due to numerical errors. Thus, it is desirable to find alternative symmetric representations. In the non-relativistic second-order differential equation this can be achieved by re-mapping the eigenfunctions before the Fourier grid method is applied [5]. While this approach guarantees real eigenvalues, it is also possible to lose efficiency as the introduced effective potential has a more complicated structure than the original one.

For the present case of coupled first-order differential equations we have not been able to find a symmetric representation without a huge gain in numerical complexity. We demonstrate, however, that the use of the non-symmetric representation introduced in equation (16) does not present a practical problem for a wide range of reasonable parameters N and s. The

Hamiltonian matrix is found to be diagonalizable with real-valued eigenenergies, and linearly independent eigenvectors.

For inappropriate choices of s, namely when s is so large at given N that the coordinate mesh becomes too sparse, numerical artefacts cause the eigenvalues to acquire imaginary parts. Increasing the number of grid points N, or increasing the numerical precision will resolve the problem. The range of s, for which the Hamiltonian is properly diagonalizable, spans calculations with no bound states to calculations where all positive-energy states are bound states. Examples of the ranges for calculations of different size are shown in the figures and discussed in the following section.

The Hamiltonian matrix has many benefits that contribute to the computational efficiency: (i) the potential terms are simply evaluated on the mesh, (ii) the derivative terms are calculated without numerical differencing, (iii) as the D matrix depends only on the parameter N, it needs to be calculated only once for a given N and can be reused when changing either the scaling parameter, or the angular momentum quantum number, or the nuclear charge Z. The numerical order of the method is controlled primarily by the diagonalization, i.e. it scales as $(2N)^3$ [15].

3. Results

The method yields reasonably accurate eigenvalues with about 100 mesh points and displays incremental improvement if the number of points is doubled in this regime. The scaling parameter s, allows for flexibility in the calculation; therefore, results pertaining to the accuracy of the eigenvalues and eigenvectors will be shown as functions of s. These accuracies and the number of bound states obtained, N_b, depend on the choice of κ, but the trends are common to all κ. For larger values of κ the region near the nucleus becomes less important. This is analogous to the Schrödinger–Coulomb problem where the centrifugal potential suppresses the probability density at small r for higher values of the orbital angular momentum l. Independent of s, the spectrum of the Hamiltonian contains continuum states with positive and negative-energy eigenvalues. These do not come in equal numbers due to the presence of the bound states.

Before going into details of specific calculations for several κ values some general trends are illustrated. The number of bound states obtained, N_b, increases as s and N increase. This is shown in figure 1 for $|\kappa| = 1$ with $N = 32$, $N = 64$ and $N = 128$. As N_b approaches N the s-ranges for which N_b stays constant, increases. For smaller $|\kappa|$, more bound states are obtained. In the case of $N = 64$, $|\kappa| = 1$ around half of them have a relative error of less than one permil for the first half of the s-range. The rest-mass energy has been subtracted from the energy eigenvalue in the calculation of the relative error to provide a more accurate measure.

The coverage of the positive- and negative-energy-continuum parts of the spectrum of the Hamiltonian changes with s and N. For the positive continuum, as s increases the spectrum bunches up around $E = +mc^2$, as shown in figure 2 for $N = 20$, $|\kappa| = 1$. The level shown at the bottom represents the $n = 3$ bound state and remains constant while the higher continuum states decrease as s increases. Each eigenvalue decreases continuously towards the $E = mc^2$ boundary as s increases. This decrease creates a higher density of states near the boundary as s increases.

Since the energy spectra are equal for $\kappa = \pm 1$, the density of calculated eigenvalues depends on $|\kappa|$ only. As $|\kappa|$ increases the rate of descent of the high continuum states increases. As N is increased the number of states increases, while their rate of descent decreases yielding a more complete coverage of the continuum. There is no simple relation between the distribution of continuum states for different N values, e.g., doubling N will
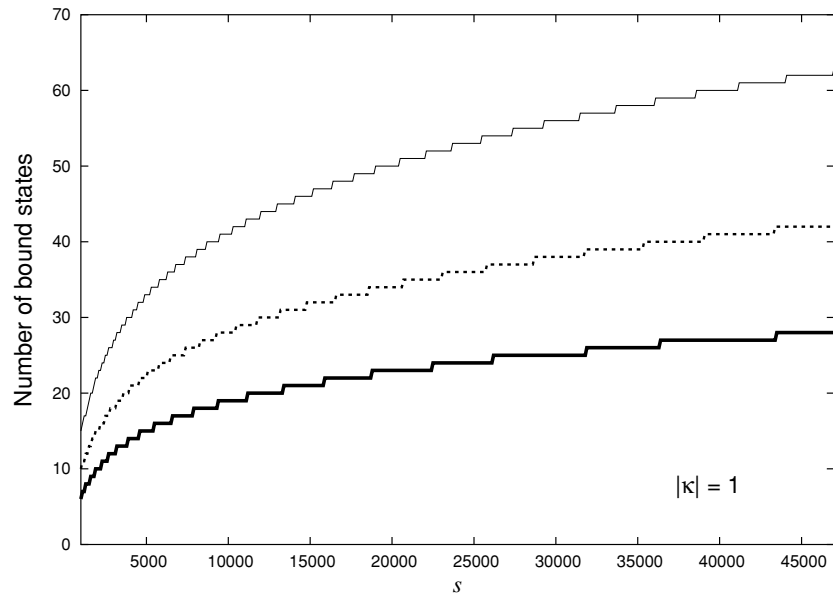
Figure 1. The number of $|\kappa| = 1$ bound states obtained by the diagonalization of the Hamiltonian matrix as a function of s for $N = 32$ (thick line), $N = 64$ (dashed line) and $N = 128$ (thin line).
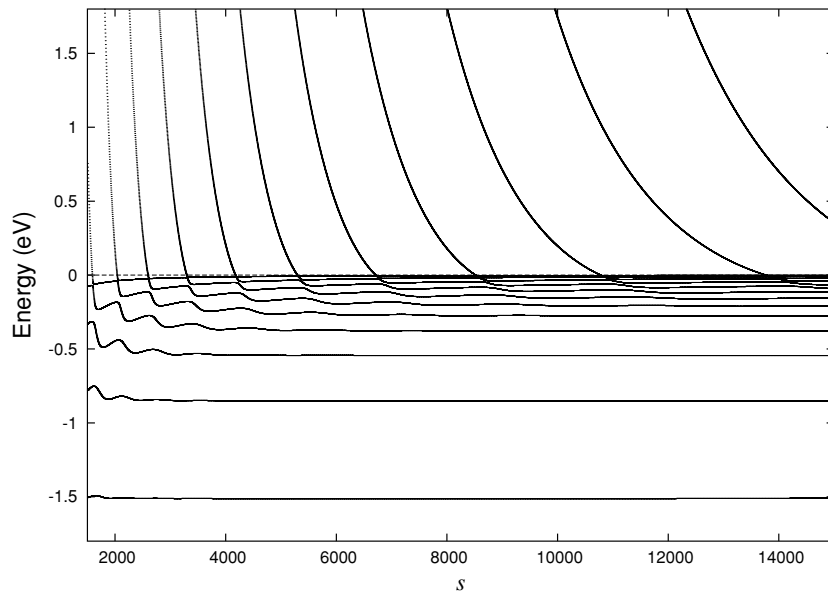

Figure 2. Distribution of some of the calculated positive-energy eigenvalues as a function of s for $N = 20$, $|\kappa| = 1$. The dotted line represents the continuum boundary and each solid line represents an energy eigenvalue obtained at that value of s.

not necessarily cause an additional continuum state to appear in between each given pair of states. Note how figure 2 displays avoided curve crossings as the Hamiltonian matrix depends parametrically on s [16].
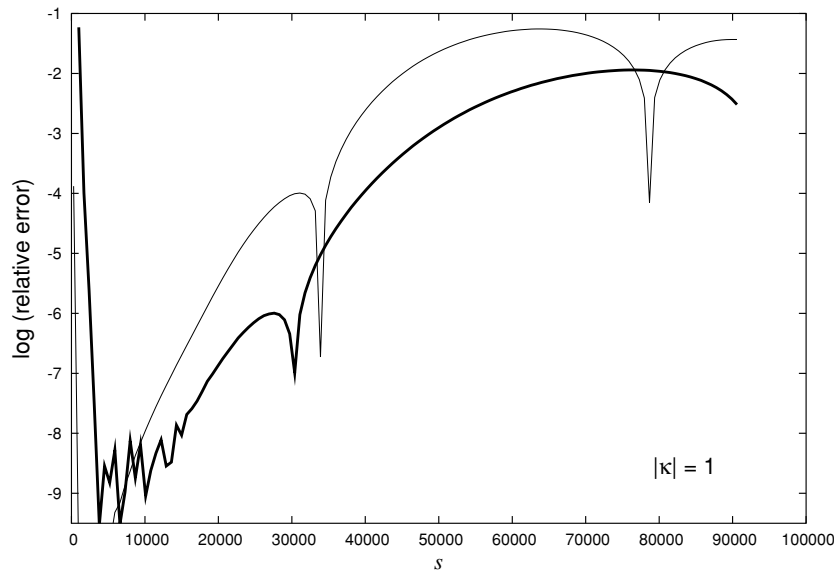
Figure 3. Logarithm of the relative error in the $|\kappa| = 1$, $n = 1$ (thin line) and $n = 6$ (thick line) eigenvalues as a function of the s for $N = 64$. The rest-mass energy was subtracted before the error calculation.

The negative-energy-continuum states behave in an analogous fashion with the exception that they cannot cross the $E = -mc^2$ boundary. The distribution of states is comparable for the continuum states at the two extremes of the spectrum, and slightly different for the states near $E = +mc^2$ and $E = -mc^2$ given that some of the positive-energy states become bound states with increasing s. In any calculation one-half of the states obtained are negative-energy-continuum states, while the remaining half is divided into positive-energy-continuum states and bound states.

The accuracy of the bound-state eigenenergies depends on the specific choice of quantum numbers and parameters, but some general observations can be made. As s increases the error in the energy eigenvalue reaches a minimum and then starts to increase as shown in figure 3 for the $n = 1$, and $n = 6$ states for $|\kappa| = 1$, where n is the relativistic analogue of the principal quantum number. Once the scaling parameter becomes large, the $n = 1$ state is no longer properly represented, as there are too few mesh points at small r to resolve it. Thus, the relative error in the energy eigenvalue increases. For high s values it is evident that some of the lower bound states become less accurate than some of the higher ones. Once the chosen mesh is ideally suited for representing a particular bound state, the error is limited by numerical noise due to finite-precision arithmetic. The $n = 6$ state reaches its numerical noise limit at a higher relative error than the $n = 1$ state. It is generally true that for higher n the numerical noise limit is higher. The graphs are truncated at the bottom when data reach the level of numerical noise.

When a bound state first appears (as shown for the $n = 6$, $\kappa = -1$ state in figure 3 at around $s = 500$), it really represents a part of the Rydberg series and so the error of the energy eigenvalue is large. This is due to the lack of points to resolve the largest anti-node properly. We call such a state a pseudo-Rydberg state. As the scaling parameter is increased, the state becomes a true bound state, and new pseudo-Rydberg states appear. For the $n = 6$, $|\kappa| = 1$ state in figure 3 this occurs at $s \approx 3000$. The value of s is now large enough to warrant a proper resolution of the largest lobe for the $n = 6$ bound state.
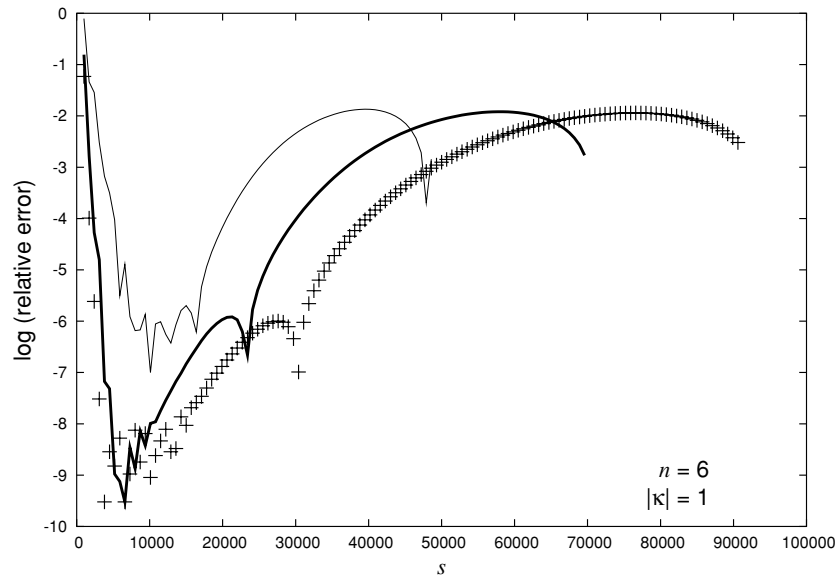
Figure 4. Logarithm of the relative error for the $n = 6$, $|\kappa| = 1$ eigenvalue (without rest energy) as a function of s for $N = 32$ (thin line), $N = 48$ (thick line) and $N = 64$ (points).

For $N > 64$ the maximum accuracy of almost every good energy eigenvalue is at the level of numerical noise. In figure 4 the s-dependence of the accuracy of the energy eigenvalue for the $n = 6$, $|\kappa| = 1$ state is shown for different N values. With increasing N the relative error reaches a lower minimum at higher s values, eventually approaching the level of numerical noise. Additionally, increasing N has the effect of decreasing the rate with which the error increases with s after the minimum error. Figure 4 also illustrates how s_{max} (the largest value of s that guarantees all eigenvalues to be real) is related to N. When N is increased the curve reaches a higher value of s_{max}, which is related nonlinearly to s.

As the accuracy of the energy eigenvalue increases, the eigenvector approaches the exact values evaluated at the mesh points. A measure of the accuracy of the spinor itself, which is represented by the eigenvector, is given by the verification of the relativistic sum rules [17]

$$\int_0^\infty g^2 \, dr = \frac{1}{2}(1 + E), \tag{17}$$

$$\int_0^\infty f^2 \, dr = \frac{1}{2}(1 - E), \tag{18}$$

$$\int_0^\infty fg \, dr = \frac{\kappa}{2\alpha Z}(1 - E^2), \tag{19}$$

$$\int_0^\infty fgr \, dr = \frac{1}{4}(2\kappa E - 1), \tag{20}$$

$$\int_0^\infty \left(\frac{g^2 - f^2}{r}\right) dr = \frac{1}{\alpha Z}(1 - E^2), \tag{21}$$

given in relativistic units. The relative error in the sum rules as a function of s follows the trend of those for the corresponding energy eigenvalue and is shown in figure 5.
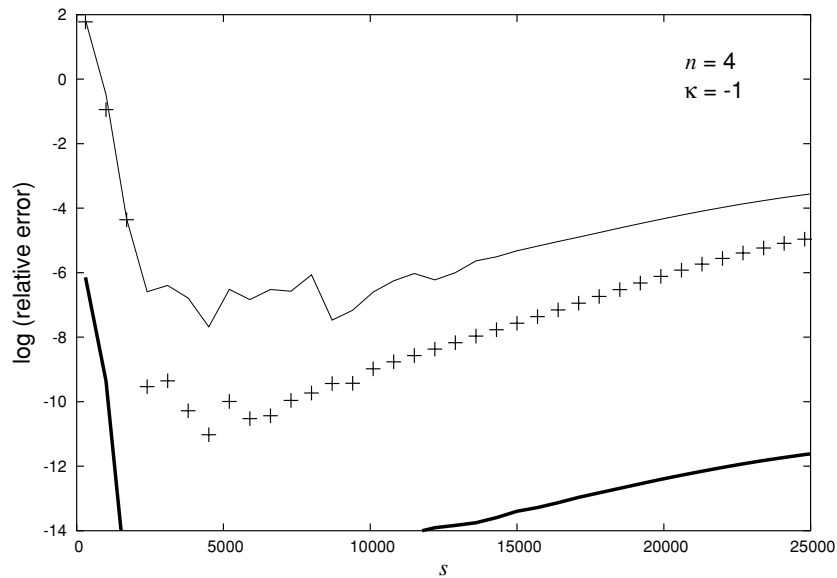
Figure 5. Logarithm of the relative error in the $n = 4, \kappa = -1$ state for $N = 64$. The three sum rules given in equation (18), (19) and (21) are jointly represented by the thin line. Results for the eigenvalue error coincide with those for equation (20) and are represented by the points, while results for the sum rule equation (17) are represented by the thick line.

3.1. Results for some $\kappa = -1$ eigenvectors

The eigenvectors become more accurate as the error in the energy eigenvalues decreases, as seen in figure 5 for the $n = 4$ state calculated with $N = 64$ using the sum rule criteria. While the relative error for the sum rules given in equations (18), (19) and (21) only approaches about 10^{-7}, this represents the achievable accuracy for those computations, since it is at their level of numerical noise. This is evident from the random pattern of points for $s \gtrsim 2000$. For lower N values these curves show improvement when the number of points is increased until around $N = 50$. Around this value for N, the optimal accuracy cannot be improved further within 16-digit floating-point arithmetic. For errors at the level of numerical noise, an increase of N does expand the range of s in which the error does not increase.

Increasing N also decreases the rate at which the eigenvector error grows with s, at high s values. While the mesh is stretched by the increased scaling parameter, there are also more points available to represent the oscillatory part of the function. In figure 6 the upper component's oscillatory part of the $n = 4$ state is shown for both $N = 64$ and $N = 128$ for $s = 20\,000$ (for the relative error cf figure 5). The remainder of the state, not shown in the figure, is represented by more than $N/2$ points in both cases. All bound states decay exponentially, but this cannot be represented accurately in the Fourier basis, which affects the sum rule calculation.

Using the exact expressions for the hydrogenic wavefunctions it is possible to calculate the relative error for each mesh point. This is shown in figure 7 for the $n = 4, \kappa = -1$ state. The graph illustrates several features of the solution obtained by the pseudospectral method: (i) increasing N has a significant impact on the accuracy of the representation of the eigenvector, (ii) the exponentially decaying tail of the wavefunction is not represented well at large r and (iii) the nodes give uncharacteristically high relative error due to the definition
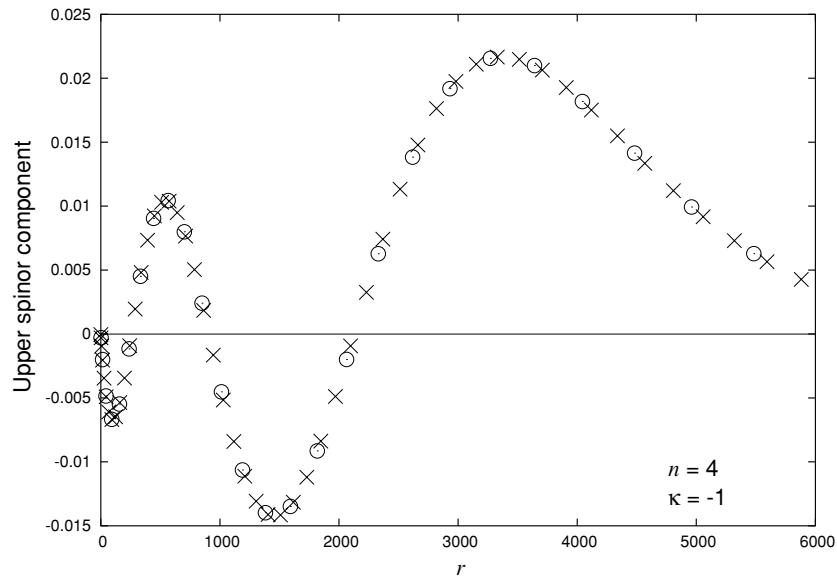
Figure 6. The oscillatory part of the upper component of the $n = 4, \kappa = -1$ spinor for $s = 20\,000$ with $N = 64$ (circles) and $N = 128$ (crosses), where r is in units of $\hbar/mc$.
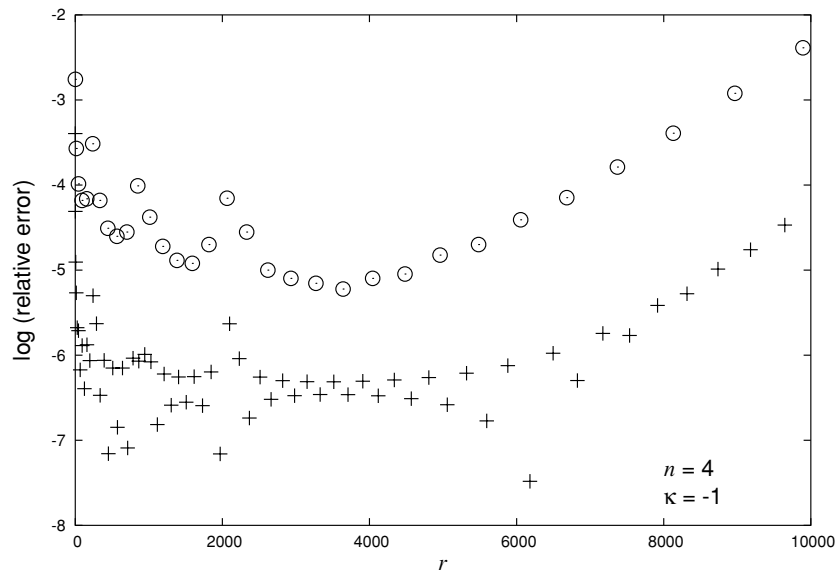

Figure 7. The relative error in the upper component of the $n = 4, \kappa = -1$ spinor for $s = 20\,000$ evaluated at the mesh points for $N = 64$ (circles), and $N = 128$ (crosses), where r is in units of $\hbar/mc$.

of the relative error. For the remainder of the graph which is not shown ($r > 10\,000$) the error continues to increase. The cause of the decrease in the accuracy of states as s increases (as was shown in figure 5), is due to more points being placed at large r which contain the inaccurately represented tail of the eigenfunction. The deficient representation of the exponentially decreasing tail is unavoidable in the Fourier-sine representation.
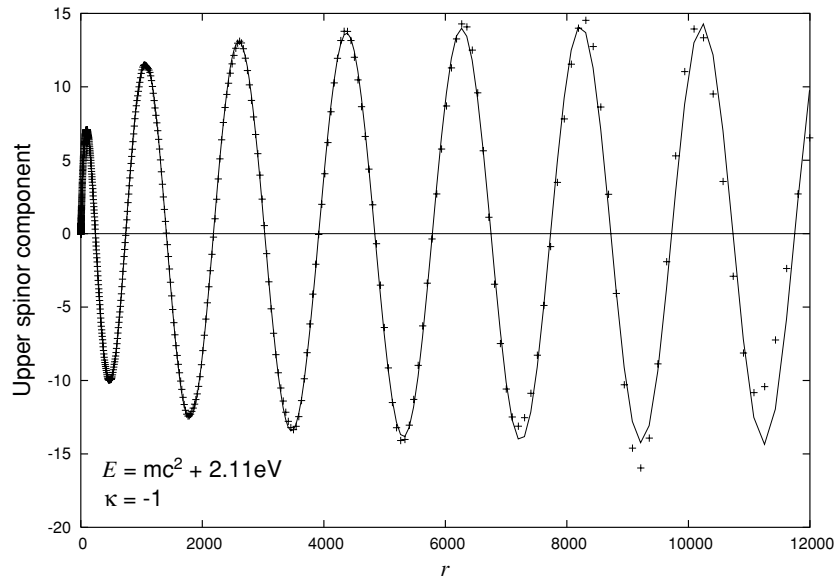
Figure 8. The calculated upper component of a $E = mc^2 + 2.11\,\text{eV}$ continuum state for $\kappa = -1, N = 128, s = 5000$ is masked by crosses; solid line: exact answer; r is in units of $\hbar/mc$.

The positive-energy-continuum states are in good agreement with the analytic solutions for $r \lesssim 4000$ as shown in figure 8 for the upper component of a state with $E = 2.11\,\text{eV}$. As r increases the approximation to the eigenfunction gets worse due to the increased spacing of the collocation points. This eventually leads to the aliasing problems. For continuum states of higher energy the local wavenumber increases and the aliasing problems occur at smaller r-values.

The negative-energy-continuum states agree well with the analytic solution only after the first antinode as shown in figure 9 for the lower component of a state with $\triangle E = -2.01\,\text{eV}$ below $-mc^2$. The lower component is shown since it is large for negative-energy states. We note a rapid oscillation of the points near the origin. This becomes less of a problem for larger $|\kappa|$. The remainder of the graph behaves in much the same way as the positive continuum state becoming more inaccurate and eventually leading to the aliasing of the function. It should be noted that the range for which the state is a good approximation of the analytic solution is fairly large, namely we can expect the continuum states to be accurate in those regions of r-space where the bound states are properly resolved.

The energy eigenvalues for $\kappa = 1$ are equal to those of $\kappa = -1$ and so their accuracies are equal. The eigenvectors are also equally accurate for $\kappa = \pm 1$ with only slight variations depending on which sum rule is used.

3.2. Spurious roots

Matrix representations of the Dirac equation are known to be plagued by the appearance of spurious roots for $\kappa \geqslant 1$ [18, 19]. This is related to the symmetric treatment of the large and small components, the dependence of the structure of the matrix representation on $|\kappa|$, while the true spectrum of bound states in the Dirac equation is different for the case of $\kappa > 0$ and $\kappa < 0$. The spurious root with an energy value in $\kappa \geqslant 1$ spectra corresponding to the lowest
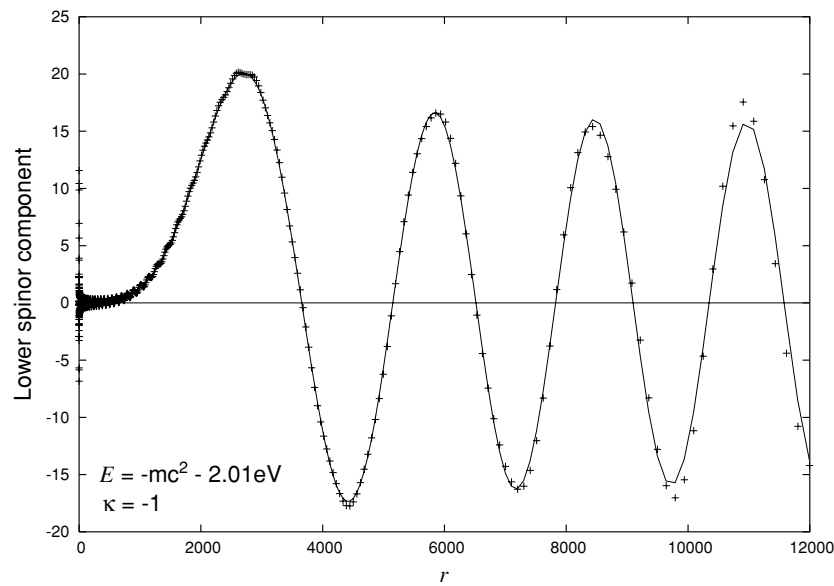
Figure 9. The calculated lower component of a continuum state located $\triangle E = -2.01$ eV below $-mc^2$ for $\kappa = -1$, $N = 128$, $s = 5000$ is marked by crosses; solid line: exact analytic answer; r is in units of $\hbar/mc$.

$\kappa < 0$ eigenvalue can be avoided by construction in explicit finite-basis set calculations [20]. In our Fourier-sine representation it is unavoidable: e.g. the spurious root for $\kappa = 1$ has an energy eigenvalue equal to the $\kappa = -1$ ground state. The large and small components of the eigenvector that correspond to this state are given by a series of alternating points that are largest near the ends of the r-range. From these properties the state is clearly identifiable as a non-physical state. In the Fourier grid representation of the Schrödinger problem in [7] an apparently similar phenomenon of non-physical roots was observed (so-called ghost states). These states appeared in somewhat random locations. They appear to be associated with properties of the coordinate mapping. The Dirac spurious roots, however are related to the boundary condition for the small component at $r = 0$.

3.3. Results for the $\kappa = -2$ states

The behaviour of the energy eigenvalues and the eigenvectors for the $\kappa = -2$ states is similar to the $\kappa = -1$ states as shown in figure 10. The eigenvectors for this symmetry remain more accurate for larger ranges of s than for the $\kappa = -1$ symmetry. It is generally observed that the larger $|\kappa|$ is, the larger the range of s in which the accuracy will remain optimal. This is analogous to the trend in the energy eigenvalues and also follows the behaviour that higher N values yield an increased range in which the error is at the level of numerical noise.

3.4. Orthogonality of the eigenvectors

The inner product of any two distinct eigenvectors is expected to be zero, since they represent eigenvectors of a self-adjoint operator in Hilbert space. The radial integral is approximated by a finite sum terminating at r_{max} which depends on N and s. Thus, the inner product in Hilbert space is replaced in the matrix representation by finite sums with features stemming from the finiteness of the representation. In order to test for orthogonality the relative angles
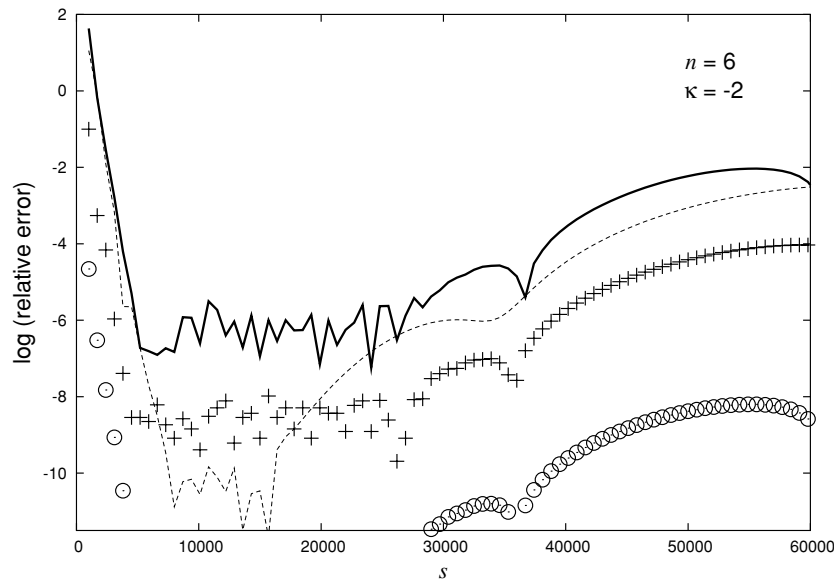
Figure 10. Logarithm of the relative error for the $n = 6, \kappa = -2$ state. The solid line is the result for equations (18) and (19), the dashed line for equation (20), the circle for equation (17) and the crosses for the energy eigenvalue (with the rest mass subtracted).

were calculated for eigenvector pairs. We chose as a measure for acceptable orthogonality a maximally allowed deviation in angle of $|\triangle\theta| = 1°$ from $90°$. For $N = 64, |\kappa| = 1$ and $300 < s < s_{max}$ states, the criterion was satisfied by more than 95% of the pairs and for $N = 128, |\kappa| = 1$ and $300 < s < 74\,000$ by more than 97%. For larger $|\kappa|$ the situation improves, e.g., for $N = 128, |\kappa| = 16$ and $300 < s < 74\,000$ more than 98% satisfy the criterion. We note that the problematic eigenvectors correspond to continuum states of high energy. In general, the bound states satisfy orthogonality better than when evaluating the inner product for the exact function while truncating the integral at r_{max}. The orthogonality condition is stable with respect to variations in s.

A larger value of s produces more low-energy continuum states (cf figure 2) which satisfy the orthogonality criterion. For the bound states an increase of s causes more pseudo-Rydberg states to become accurate bound states and therefore their mutual orthogonality improves.

3.5. Effects of different Z

All trends previously stated apply also to the cases with $Z > 1$. The number of bound states as a function of s is shown in figure 11 for $Z = 92$ with $|\kappa| = 1$. For larger Z the relevant radial distance range decreases. This causes the calculation to be much more sensitive to s, and it even becomes possible to choose s sufficiently large such $N_b = N$. This is shown in figure 11 for both the $N = 32$ and $N = 64$ calculations where both reach $N_b = N$ for $s \lesssim s_{max}$. The accuracies of the energy eigenvalues and eigenvectors for states with $|\kappa| \neq 1$ give similar results as those above, reaching the numerical noise limit in accuracy for $N \approx 64$. The $\kappa = \pm 1$ symmetries follow the same trends, but one is unable to approach the numerical noise limit with the same number of points. The $Z = 92$ hydrogenic problem requires $N \gtrsim 128$ for the $|\kappa| = 1$ states in order to reach minimal error at the level of numerical noise.
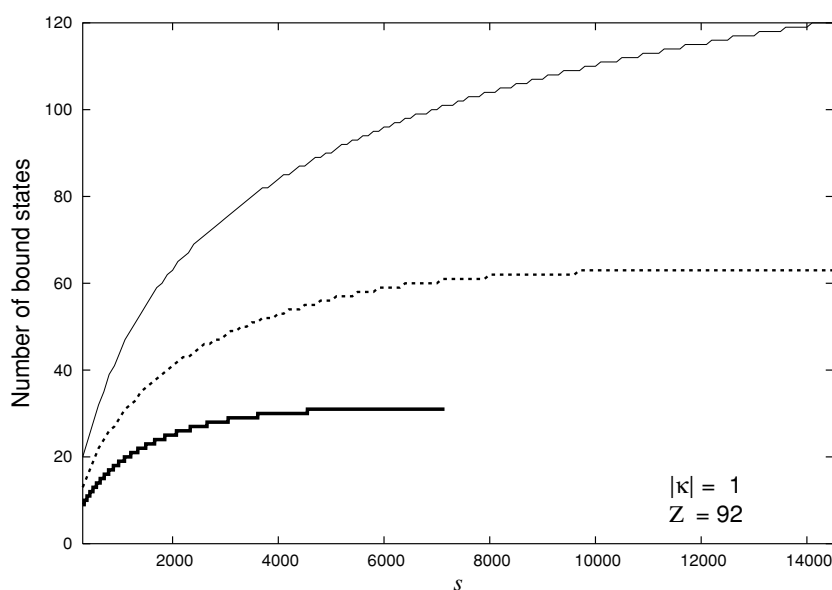
Figure 11. The number of $|\kappa| = 1$, $Z = 92$ bound states obtained by the diagonalization of the Hamiltonian as a function of s for $N = 32$ (thick line), $N = 64$ (dashed line) and $N = 128$ (thin line).

4. Discussion

The mapped Fourier method has been applied successfully to the Dirac–Coulomb problem. It yields accurate results with a moderate number of mesh points. Using the scaling parameters it is possible to tailor the spectrum of the Hamiltonian matrix. This feature, as well as the precalculation of the derivative terms, suggests that this representation technique is well-suited for time-dependent problems for which a representation of continuum states is important. Although in this work a pure Coulomb potential was used, the method can be applied to other spherically symmetric potentials. Due to the direct implementation in coordinate space with a built-in interpolation scheme for r-values in between mesh points the method is ideally suited for self-consistent field calculations as they arise in density functional theory [2].

References

  [1] Parpia F A, Fisher C F and Grant I P 1996 *Comput. Phys. Commun.* **94** 249
  [2] Engel E, Keller S, Bonnetti A F, Müller H and Dreizler R M 1995 *Phys. Rev.* A **52** 2750
  [3] Braun J W, Su Q and Grobe R 1999 *Phys. Rev.* A **59** 604
  [4] Becker U, Grün N, Scheid W and Soff G 1986 *Phys. Rev. Lett.* **56** 2016
  [5] Kokoouline V, Dulieu O, Kosloff R and Masnou-Seeuws F 1999 *J. Chem. Phys.* **110** 9865
  [6] Marston C C and Balint-Kurti G G 1989 *J. Chem. Phys.* **91** 3771
  [7] Willner K, Dulieu O and Masnou-Seeuws F 2004 *J. Chem. Phys.* **120** 548
  [8] Meyer R 1970 *J. Chem. Phys.* **52** 2053
  [9] Fattal E, Baer R and Kosloff R 1996 *Phys. Rev.* E **53** 1217
  [10] Boyd J P, Rangan C and Bucksbaum P H 2003 *J. Comput. Phys.* **188** 56
  [11] Alberto P, Fiolhais C and Gil V M S 1996 *Eur. J. Phys.* **17** 19
  [12] Kleinekathöfer U and Tannor D J 1999 *Phys. Rev.* E **60** 4926
  [13] Greiner W 2000 *Relativistic Quantum Mechanics: Wave Equations* 3rd edn (Berlin: Springer)
  [14] Sakurai J J 1984 *Advanced Quantum Mechanics* (New York: Addison-Wesley)

[15] Press W H, Teukolsky S A, Vetterling W T and Flannery B P 1992 *Numerical Recipies in C* (Cambridge: Cambridge University Press)
[16] Hatton G J 1977 *Phys. Rev.* A **16** 1347
[17] Goldman S P and Drake G W F 1982 *Phys. Rev.* A **25** 2877
[18] Kutzelnigg W 1984 *Int. J. Q. Chem.* **25** 107
[19] Krauthauser C and Hill R B 2002 *Can. J. Phys.* **80** 181
[20] Goldman S P 1985 *Phys. Rev.* A **31** 3541